


RESEARCH

Open Access



# Wearable synthetic leather-based high-performance X-ray shielding materials enabled by the plant polyphenol- and hierarchical structure-facilitated dispersion

Linping Yan<sup>1</sup>, Jibo Zhou<sup>1</sup>, Hao Li<sup>1</sup>, Rui Zhong<sup>3</sup>, Junxin Zhuang<sup>4</sup>, Xiaohui Xu<sup>5</sup>, Yaping Wang<sup>1,2\*</sup> , Xuepin Liao<sup>1,2</sup> and Bi Shi<sup>1,2</sup>

## Abstract

Effective protection against X-ray is the premise of utilizing the X-ray, thus it is critical to develop novel X-ray shielding materials with both low density and high X-ray attenuation efficiency. As the even distribution of high-Z element components is of great significance for increasing the attenuation efficiency of X-ray shielding materials, in this study, the microfibrillar membrane (MFM), a type of synthetic leather featuring hierarchical structure was chosen to provide large surface area for the dispersion of rare earth (RE) element. Meanwhile, plant polyphenol was utilized to achieve the stable loading and uniform dispersion of the Ce or Er into MFM. Benefiting from the assistance of polyphenol and hierarchical structure of MFM, the even dispersion of RE element was successfully realized. The resultant shielding materials displayed approximately 10% superior X-ray attenuation efficiency compared to that without polyphenol, and an averagely 9% increment in X-ray attenuation efficiency than that without hierarchical structure. Moreover, the obtained composite with a thickness of 2.8 mm displayed superior X-ray shielding performance compared to 0.25 mm lead sheet in 16–83 keV and retained an ultralow density of 1.4 g cm<sup>-3</sup>. Our research results would shed new light on the manufacture of high-performance X-ray shielding materials with excellent X-ray shielding performance.

**Keywords** X-ray shielding, Plant polyphenol, Microfibrillar membrane, Synthetic leather, Hierarchical structure, Dispersity

\*Correspondence:

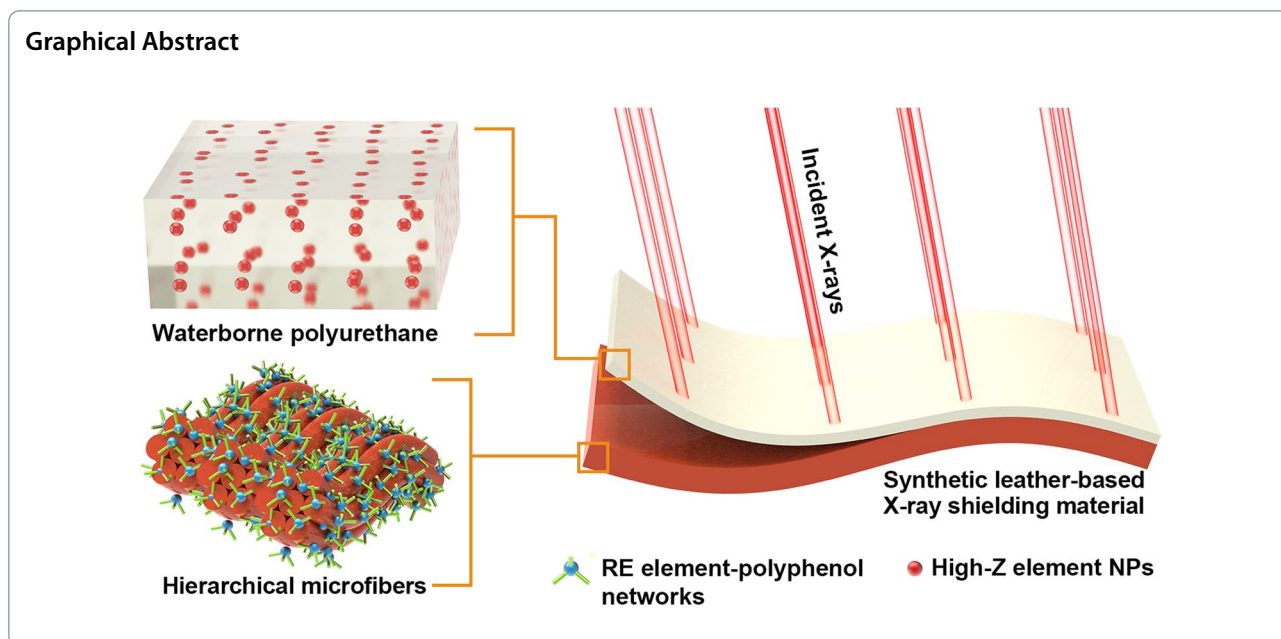
Yaping Wang

ypwang@scu.edu.cn

Full list of author information is available at the end of the article



© The Author(s) 2023. **Open Access** This article is licensed under a Creative Commons Attribution 4.0 International License, which permits use, sharing, adaptation, distribution and reproduction in any medium or format, as long as you give appropriate credit to the original author(s) and the source, provide a link to the Creative Commons licence, and indicate if changes were made. The images or other third party material in this article are included in the article's Creative Commons licence, unless indicated otherwise in a credit line to the material. If material is not included in the article's Creative Commons licence and your intended use is not permitted by statutory regulation or exceeds the permitted use, you will need to obtain permission directly from the copyright holder. To view a copy of this licence, visit <http://creativecommons.org/licenses/by/4.0/>.



## 1 Introduction

X-ray is a kind of high-energy electromagnetic radiation widely employed in a variety of fields, such as medical diagnosis, material characterization, fouling control, and defect detection [1–4]. As prolonged exposure to X-ray can cause biochemical, carcinogenic, and genetic injuries that seriously affect human health [5, 6], it is of great significance to protect the human body from exposure to X-ray. As X-ray primarily interacts with matters via the photoelectric effect and Compton scattering, in which the interaction probabilities of each effect are positively correlated to the atomic number ( $Z$ ) and the number of electrons, respectively [7, 8], high- $Z$  elements such as lead ( $Z=82$ ) are preferred to be utilized in X-ray shielding. However, lead suffers from poor wearability [9], hampering its applications in a wide range of mobile scenarios. Therefore, it is vital to develop high-performance X-ray shielding materials to guarantee personal safety.

To prepare wearable X-ray shielding materials, high- $Z$  elements are commonly dispersed into polymer substrates to reduce weight. Aral et al. mixed tungsten with silicone rubber and coated them on the cotton fabrics to prepare X-ray shielding materials. The density of the obtained composite was successfully reduced to  $2.55 \text{ g cm}^{-3}$  by dispersion of high- $Z$  element, meanwhile, the composite could shield 30% of 100 kVp X-ray [10]. Muthamma et al. utilized a solution casting technique to load and disperse bismuth into poly(vinyl alcohol) to fabricate X-ray shielding materials, and the resultant composite exhibited low density of  $1.61 \text{ g cm}^{-3}$  and a mass attenuation coefficient of  $1.57 \text{ cm}^2 \text{ g}^{-1}$  at 59.54 keV [11].

Jaiyen et al. dispersed  $\text{BaSO}_4$  into polyvinyl chloride to obtain shielding materials, the density of obtained composite which containing 60%  $\text{BaSO}_4$  was  $2.36 \text{ g cm}^{-3}$ , and the mass attenuation coefficient could reach  $5.98 \text{ cm}^2 \text{ g}^{-1}$  at 50 keV [12].

Many researches have shown that the X-ray shielding efficiency is significantly influenced by the dispersity of high- $Z$  elements in the composite matrix and the hierarchical structure of substrate could contribute to the dispersion of functional components [13–16]. Quan et al. prepared polymer-matrix composites containing Bi nanoparticles and UHMWPE for personal radiation shielding, but Bi nanoparticles dispersed unevenly in UHMWPE without hierarchical structure, resulting in the difference of shielding performance [17]. Wang et al. and Shen et al. creatively loaded high- $Z$  elements into natural leather which possesses hierarchical structure, achieving high dispersion of high- $Z$  elements and obtaining excellent wearable shielding materials, while the limited size of natural leather makes it difficult to fabricate large size shielding materials [18–20]. Therefore, it is essential to search for a substrate featuring not only hierarchical structure but also adjustable size. Microfiber membrane (MFM), a type of synthetic leather, possesses hierarchical porous structure, the softness and low density, and has been broadly applied to prepare wearable clothing such as synthetic leather coats and shoes [21]. Particularly, MFM exhibits highly regular structure and adjustable spread area which is versatile for various application scenarios. Originating from the hierarchical porous structure, larger specific surface area could be

used to load and disperse high-Z element in the MFM, increasing loading amount of high-Z element on the microfiber surface and improving the X-ray shielding performance. Thereby, it is promising to utilize the hierarchical structure of MFM to enhance X-ray shielding performance.

Furthermore, stable loading and even dispersion of high-Z element are also beneficial to improving X-ray shielding efficiency. Plant polyphenol, a natural plant extract, could adhere to the surfaces of various substrates through covalent or noncovalent bond, providing more active groups as reaction sites on the surface to react with high-Z element. Meanwhile, it contains plenty of phenolic hydroxyls which can coordinate with most metal ions to form steady metal–phenolic networks (MPN) [22]. Hence, it is intriguing to apply the strong adhesion of polyphenol to load and disperse high-Z element steadily on the microfiber surface to improve X-ray shielding efficiency in the preparation of microfiber membrane-based materials.

Based on the aforementioned analysis, we reported a new strategy for preparing X-ray shielding materials by using polyphenol as a bridge to load and disperse high-Z element stably into MFM. The novel X-ray shielding materials based on MFM were prepared successfully via the improved “impregnation–desolvation” strategy. MFM featuring the hierarchical structure was selected as the substrate to load and disperse RE element, and the loading stability and dispersity of RE element were significantly enhanced with the help of the plant polyphenol, resulting in remarkable enhancement of the X-ray shielding performance of the prepared samples. Thus, novel approaches to manufacture high-performance X-ray shielding materials based on polymer fabrics were proposed through this study.

## 2 Experimental section

### 2.1 Materials

Erbium nitrate pentahydrate ( $\text{Er}(\text{NO}_3)_3 \cdot 5\text{H}_2\text{O}$ ) and cerium nitrate hexahydrate ( $\text{Ce}(\text{NO}_3)_3 \cdot 6\text{H}_2\text{O}$ ) were obtained by Aladdin Bio-Chem Technology Co., Ltd. (Shanghai, China). Barium carbonate ( $\text{BaCO}_3$ ) and bismuth trioxide ( $\text{Bi}_2\text{O}_3$ ) nanoparticles were purchased from Yaotian Nano New Materials Co., Ltd. (Shanghai, China). Bayberry tannin (BT, extracted from the bark of bayberry) was obtained by Tianxing Plant Technology Co., Ltd. (Guangxi, China). Acetone was purchased from Kelong Chemical Co., Ltd. (Sichuan, China). All the chemicals were of analytical grade and were used as received. Microfiber membrane (MFM, 1.2 mm thick) was kindly provided by Mingxin Menoroka New Material Co., Ltd. (Jiangsu, China). Woven polyethylene terephthalate fabric membrane (PETM, 1.2 mm thick) was

purchased from Suzhou Renfeng Textile Technology Co., LTD. (Jiangsu, China). Waterborne polyurethane (WPU) was purchased from Dowell Chemical Co., Ltd. (Sichuan, China).

The microfiber membrane (MFM) was fabricated by sea-island conjugated spinning technology with a Co-PET sea and PET islands, where the microfibers were arranged randomly and fixed. Briefly, the sea-island microfibers were fixed by polyurethane, and the sea components (Co-PET) were then removed to give a piece of microfiber membrane with hierarchical structure.

### 2.2 Preparation of microfiber membrane/bis-high-Z element composites ( $\text{Z}_y\text{RE}_x\text{-MFM}$ )

Before the introduction of high-Z elements, the rare earth (RE) element salt was initially dissolved in  $0.03 \text{ g mL}^{-1}$  BT solution based on the volume of MFM to form metal–phenolic networks (MPN). The resultant samples were denoted as  $\text{RE}_x\text{-MPN}$ , where RE represents the elemental symbol of the introduced rare earth element, and  $x$  signifies the loading amount of the rare earth element in  $\text{mmol}_{\text{RE}} \text{ cm}_{\text{MFM}}^{-3}$ . Then the RE elements were introduced by the “impregnation–desolvation” strategy developed by our group [18, 19]. Briefly, a piece of MFM ( $100 \times 100 \times 1.2 \text{ mm}^3$ ) was immersed in 12 mL MPN solution for 6 h to load the RE element, and the solvent was removed by acetone, producing the intermediate samples marked by  $\text{RE}_x\text{-MFM}$ . Afterward,  $\text{BaCO}_3$  or  $\text{Bi}_2\text{O}_3$  NPs were dispersed in WPU solution with a weight ratio of 1:3, and the mixtures were then coated onto the outer surface of  $\text{RE}_x\text{-MFM}$  to form a  $1.0 \text{ mmol}_{\text{element}} \text{ cm}_{\text{MFM}}^{-3}$  coating layer, and were dried at  $60 \text{ }^\circ\text{C}$ . The obtained composites were denoted as  $\text{Z}_y\text{RE}_x\text{-MFM}$  (where Z represents the elemental symbol of the coated high-Z elements, RE symbolizes the elemental symbol of the introduced rare earth elements,  $y$  denotes the coating amount of the high-Z element in  $\text{mmol}_{\text{element}} \text{ cm}_{\text{MFM}}^{-3}$ , and  $x$  signifies the loading amount of the RE element in  $\text{mmol}_{\text{RE}} \text{ cm}_{\text{MFM}}^{-3}$ ). The same method was used to prepared control samples based on woven polyethylene terephthalate fabric membrane (PETM) with the same elemental compositions and amounts.

### 2.3 Characterizations

The coordination between BT and RE elements were confirmed by ultraviolet–visible spectroscopy (UV–Vis, UV-3600, Shimadzu, Japan), Fourier transform infrared spectrophotometry (FT-IR, Spectrum Two, Perkin-Elmer, USA), and X-ray photoelectron spectroscopy (XPS, Escalab Xi+, AXIS Ultra DLD, UK). The morphologies of MFM and  $\text{Z}_y\text{RE}_x\text{-MFM}$  were observed by field emission scanning electron microscopy (FESEM, Nova NanoSEM450, FEI, USA). Elemental distributions

of RE elements in MFM were presented by energy dispersive X-ray (EDS) mapping (EDS, Azteclive Ultim Max 100, Oxford Instruments, UK) and transmission electron microscopy (TEM, Talos F200S G2, Thermo Fisher Scientific Inc., USA). The amounts of introduced high-Z elements contents were determined using an inductively coupled plasma–optical emission spectrometer (ICP–OES, OPTIM 8000D, PerkinElmer, USA). The mechanical behaviors of MFM and the resultant composites were investigated by a universal testing machine (AI-7000 S, Gotech Testing Machines Co. Ltd., China). The samples were tailored into  $50 \times 25 \times 1.3 \text{ mm}^3$  pieces before the test. The density of composites and pore size distribution of MFM were determined by a mercury injection pore analyzer (MIP, AUTOPORE IV9500, Micromeritics Instrument, USA). The water contact angles of MFM and the resultant composites were measured by dropping a  $3.0 \mu\text{L}$  water droplet onto the surface of samples using a contact angle goniometer (DSA30, Krüss GmbH, Germany). The BET surface area of the ZRE-MFM and ZRE-PETM were measured by an automatic porosimeter (BET, ASAP 2460, USA). The fastness properties to rubbing and bending of composites were measured by a martindale abrasion testing apparatus (GC-M810-M6, Geecise Testing Machines Co. Ltd., China) and bally flexometer (2226, Jinan Xing Hua Instruments Co., Ltd., China).

#### 2.4 X-ray shielding performance tests

X-rays with different photon energies (16–118 keV) were produced by an X-ray generator (CF320, Gulmay Ltd., UK) according to the Chinese National Standard JJG 393-2003 [23]. The generated X-rays passed through the as-prepared samples, and the residual X-ray doses accumulated in 30 s were determined by a PTW-UNIDOSE dosimeter equipped with a TN34069-2,5 ionization chamber. During the X-ray shielding performance tests, the distance between the sample and the X-ray generator was 80 cm, and the distance between the sample and the X-ray detector was 20 cm. The attenuation efficiency (AE) was calculated using Eq. 1 [18]:

$$AE = \frac{I_0 - I}{I_0} \times 100\% \quad (1)$$

The linear attenuation coefficient ( $\mu$ ) was calculated by Eq. 2 [24]:

$$I = I_0 e^{-\mu d} \quad (2)$$

The mass attenuation coefficient ( $\mu_m$ ) was computed by using Eq. 3 [25]:

$$\mu_m = \frac{\mu}{\rho} \quad (3)$$

where  $I_0$  and  $I$  are the intensities ( $\text{mGy s}^{-1}$ ) of the original and transmitted X-rays,  $d$  is the thickness of the sample, and  $\rho$  is the density of the sample.

### 3 Results and discussion

#### 3.1 Preparation and characterizations of microfiber membrane/(bis-)high-Z element composites (RE-MFM and ZRE-MFM)

According to recent research, the uniform distribution of high-Z element components is of great significance for increasing the attenuation efficiency of X-ray shielding materials [26, 27], therefore, in this work, microfiber membrane (MFM) was used as the substrate to load and disperse rare earth (RE) elements. MFM is commonly used as substrate to fabricate synthetic leather, and possesses merits of both the natural leather and polymer materials. Gas absorption operation was used to obtain the specific surface area and nitrogen adsorption–desorption isotherms of MFM and PETM (Additional file 1: Figs. S2 and S3). Originating from the hierarchical structure and resultant hierarchical pores, MFM features much higher specific surface area ( $7.6 \text{ m}^2 \text{ g}^{-1}$ ) than that of commercial polyethylene terephthalate membrane (PETM,  $1.2 \text{ m}^2 \text{ g}^{-1}$ ), and may give rise to enhanced dispersion of RE elements on the microfiber surface to enlarge the probability to interact with X-ray photons. Meanwhile, to achieve the uniform dispersion of RE element, plant polyphenols were chosen as a bridge to disperse RE elements into MFM. Plant polyphenols, which are broadly employed in various industries, contain plenty of phenolic hydroxyls which can coordinate with different RE metal ions to form metal–phenolic networks (MPN) [22, 28]. What is more, polyphenols can adhere to various surfaces via the coordination, electrostatic interactions, hydrophobic interactions and hydrogen-bonding interactions. Thus, polyphenols can facilitate an effective dispersion of RE elements to form X-ray shielding composites. To achieve this goal, RE nitrate salts are firstly mixed with bayberry tannin (BT) solution to form rare earth metal–phenolic network (RE-MPN) [29]; then the RE-MPN is loaded and dispersed into the MFM by the “impregnation–desolvation” strategy to prepare the X-ray shielding materials (Fig. 1a) [18, 19]. The resultant composites are denoted as  $\text{RE}_x\text{-MFM}$ , where RE represents the elemental symbol of the introduced rare earth elements, and  $x$  signifies the loading amount of the RE element in  $\text{mmol}_{\text{RE}} \text{ cm}_{\text{MFM}}^{-3}$ ; the subscripts in the notations are omitted when their values do not affect the discussions (similarly hereinafter).

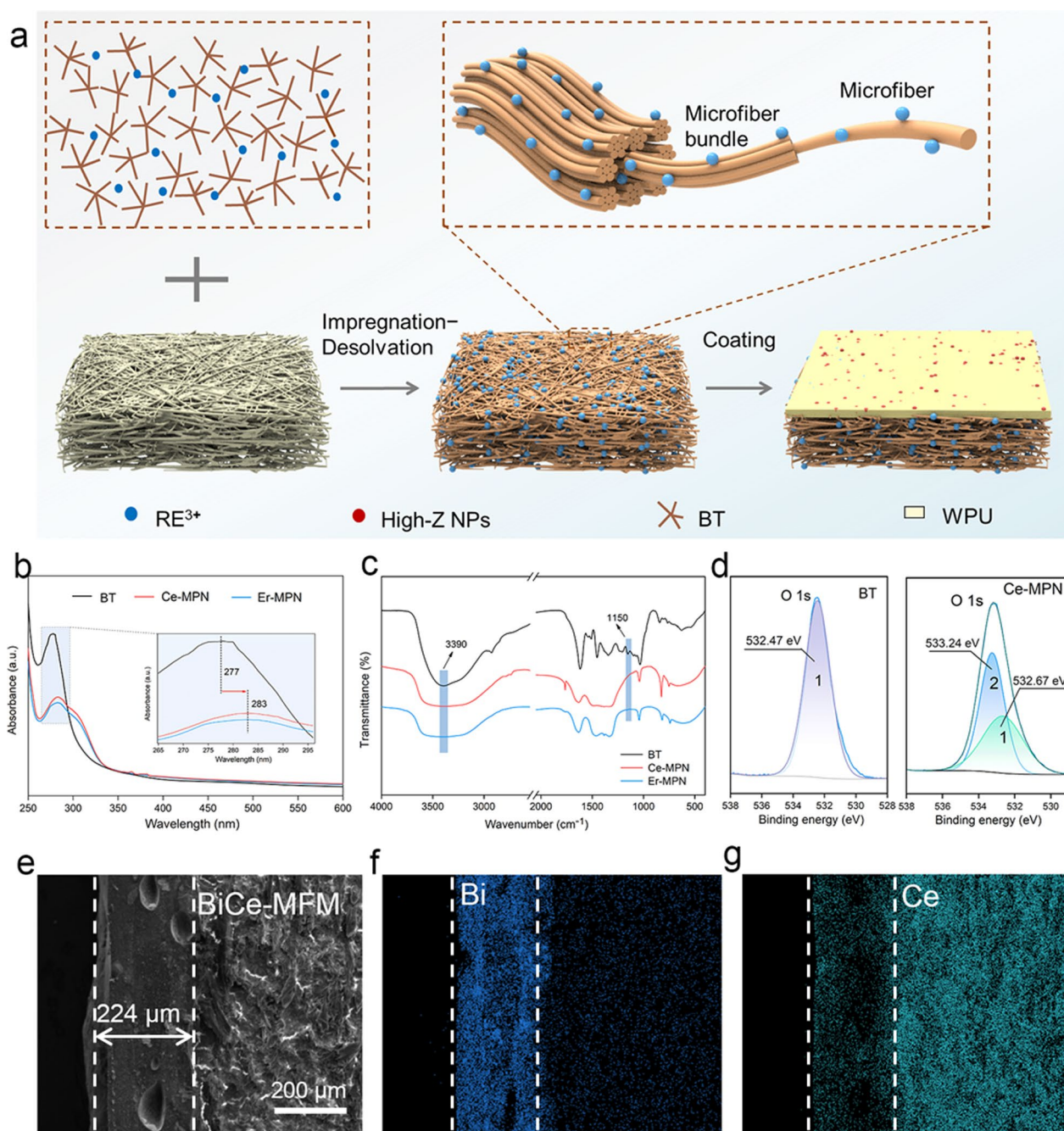


**Fig. 1** Illustrations on the preparation and characterizations of RE-MFM and ZRE-MFM. **a** Graphical illustration of the preparation process of the ZRE-MFM via the “impregnation–desolvation” strategy and then the coating process. **b** UV–Vis spectra of BT and RE-MPN. **c** FT-IR spectra of BT and RE-MPN. **d** High-resolution XPS O 1s scan spectra of BT and Ce-MPN. **e–g** SEM morphologies (**e**) and elemental mappings of Bi (**f**) and Ce (**g**) of BiCe-MFM

Furthermore, to compensate the weak absorption region of single RE element, Ba or Bi was selected to form a thin coating layer onto the surface of RE-MFM by water-borne polyurethane (WPU, Fig. 1a), and the prepared samples are named  $Z_yRE_x$ -MFM, where Z

represents the elemental symbol of the coated high-Z elements, and y indicates the coating amount of the high-Z element in  $\text{mmol}_{\text{element}} \text{cm}_{\text{MFM}}^{-3}$ .

The coordination between RE cations and phenolic hydroxyls is verified by ultraviolet–visible spectroscopy

(UV–Vis), Fourier transform infrared spectrophotometry (FT-IR) and X-ray photoelectron spectroscopy (XPS). In the UV–Vis spectrum, the maximal absorption peak of Ce-MPN has red-shifted from 277 to 283 nm as compared to BT (Fig. 1b), giving evidence for the interactions between BT and RE cations [30, 31]; additionally, the FT-IR peaks of BT at 3390 and 1150  $\text{cm}^{-1}$ , which are corresponded to O–H vibrations, have become weaker in intensity after interacting with RE cations (Fig. 1c), proving that the interactions are carried out between the phenolic hydroxyls and RE cations [32]; moreover, in the O 1s scan spectra of Ce-MPN and Er-MPN, a new peak at 533.24 eV and 533.46 eV, respectively, could be deconvoluted in comparison to BT (Fig. 1d and Additional file 1: Fig. S4), suggesting the coordination between phenolic hydroxyls of BT and RE cations [33]. In brief, the aforementioned characterizations demonstrate that plant polyphenol can coordinate with RE elements to form RE-MPN, providing the premise of dispersing RE elements into the MFM.

After introducing the RE-MPN into MFM, the second high-Z elements were appended onto the surface of RE-MFM by coating. The elemental compositions were analyzed by X-ray photoelectron spectroscopy (XPS). As shown in Additional file 1: Fig. S5, both the XPS survey spectra of BaCe-MFM and BiCe-MFM displayed Ce 3d energy peaks at 885.69 eV, and the new energy peaks located at 780.84 and 159.49 eV corresponded to the Ba 3d and Bi 4f energy levels in BaCe-MFM and BiCe-MFM, respectively, further confirming the introduction of Ba or Bi to the Ce-MFM [34, 35]. Likewise, the two high-Z elements were also successfully loaded into Er-MFM by coating (Additional file 1: Fig. S6). The loading amounts of high-Z elements were measured by inductively coupled plasma–optical emission spectrometry (ICP–OES). The average loading efficiencies of RE elements were high up to 91% (Additional file 1: Table S1), demonstrating the excellent stabilization effect of BT; and the results indicated a satisfactory average coating efficiency of 82% (Additional file 1: Table S1), proving the successful introduction of Ba or Bi. Besides, the dispersion of high-Z elements in ZRE-MFM was characterized by field emission scanning electron microscopy (FESEM). The SEM cross-sections of BiCe-MFM (Fig. 1e) indicated that no obvious microstructure could be observed in the coating layer, and no distinct phase interface existed between the coating and Ce-MFM, suggesting that the second high-Z elements were firmly loaded onto Ce-MFM. The elemental mappings exhibited that the two introduced high-Z elements both showed distinct spatial distributions in the composites (Fig. 1f and g), where Ce predominantly existed in the MFM while Ba or Bi was only distributed in the coating layer (Additional file 1: Fig. S7); in each

matrix, the corresponding high-Z elements were uniformly dispersed. The same conclusion was also attained from the SEM and mappings of ZEr-MFM (Additional file 1: Figs. S8 and S9).

### 3.2 Synergistic effect of hierarchical structure and plant polyphenol on the uniform dispersion of RE element

The dispersion of high-Z element in the shielding material greatly affects the shielding performance of the material, therefore, MFM and BT were used to load and disperse RE element to improve the dispersion in the shielding material. According to the morphological analyses, the original MFM is composed of hierarchical microfiber bundles (25  $\mu\text{m}$ ) which consists of several parallelly arranged 3- $\mu\text{m}$  microfibers, and the surfaces of the microfibers are smooth (Fig. 2a). The data of pore size and distribution of MFM prove that microfiber bundles intercross with each other to form hierarchical pores and there exists large quantities of gaps between the single fibers in microfiber bundles (Additional file 1: Figs. S10 and S11).

After loading RE-MPN into MFM, the morphologies of MFM remained unaffected where microfibers were still bundled and their overall outline was still visible, and a layer of a thin film could also be observed which formed on the microfiber surfaces (Fig. 2c). The elemental mapping of Ce displayed the same trend as the contours of the microfibers (Additional file 1: Fig. S12), indicating the successful loading and uniform dispersion of Ce on the microfibers. The loading and dispersion of Er in MFM were also verified using SEM and corresponding elemental mapping (Additional file 1: Fig. S13). On the contrary, when RE cations were directly loaded into MFM without the facilitation of BT, the RE elements were unevenly distributed and aggregated into large particles up to micrometer scale (Fig. 2b, Ce-MFM<sub>0</sub>). As the main constituent of MFM is polyethylene terephthalate which contains few active groups, the MFM is incapable of binding and stabilizing RE elements. BT, a type of plant polyphenols versatile to bind to various matters, can interact with RE elements through coordination, and can also induce strong adhesion to MFM via hydrophobic bonding between the aromatic moieties [36]. Therefore, with the help of BT, RE elements could be successfully loaded and evenly dispersed into MFM to produce RE-MFM. This idea can expand our “impregnation–desolvation” strategy to load and disperse high-Z elements into various polymer matrices either with or without active functional groups, providing promising universality to prepare X-ray shielding materials that can be applied to various mobile scenarios.

The hierarchical structure of MFM was observed in Fig. 2d–e. The woven polyethylene terephthalate

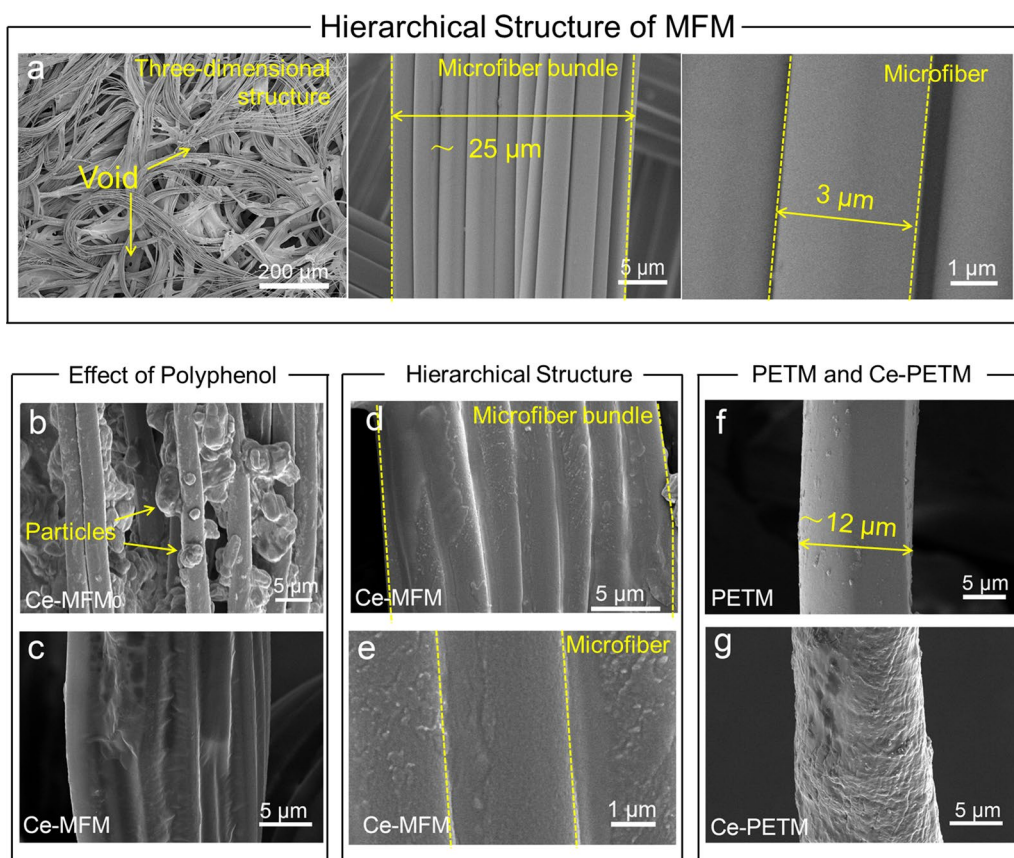


**Fig. 2** Microstructure of the prepared samples. **a** The SEM images of hierarchical structure of MFM. **b–c** The SEM images of Ce-MFM<sub>0</sub> (**b**) and Ce-MFM (**c**). **d–e** The SEM images of hierarchical structure of Ce-MFM. **f** The SEM images of single fiber of PETM. **g** The SEM images of single fiber of Ce-PETM

membrane (PETM) was selected as a controlled reference to demonstrate the merits of hierarchical structure of MFM. PETM is a typical woven fabric absent of hierarchical structure, and the single fiber's diameter was approximately 12- $\mu\text{m}$  which was 3 times larger than that of MFM (Fig. 2f and Additional file 1: Fig. S14). As seen in Fig. 2d–e, the hierarchical structure of MFM and the pores between the microfiber bundles were still present after spreading RE element onto the microfibrils surface. Meanwhile, a layer of thin film could be seen on the microfiber bundle surface, and the boundary of each microfiber was still visible, suggesting that the loading did not affect the microstructure of MFM. The microfiber surface did not exhibit any evident aggregations, indicating the uniform dispersion of RE element with the assistance of BT. Additionally, the SEM and TEM elemental mappings clearly revealed that the loaded RE elements were distributed following the direction of the fibrous structure in MFM, proving the successful loading and uniform dispersion of RE elements (Additional file 1: Figs. S15 and S16). According to Fig. 2g and Additional

file 1: Fig. S17, RE element could be loaded and dispersed on the fiber surface of PETM, suggesting the universality of plant polyphenol as bridge to disperse RE elements in the polymer matrices. Compared with PETM, the microfiber bundle of MFM has similar diameter to a single fiber of PETM, yet it consists of multiple microfibrils that is able to expose larger surface area to load and disperse RE element, enlarging the collision probability between photons and RE element. To sum up, we chose MFM with hierarchical structure as substrate to provide larger area to load and disperse RE elements, and utilized plant polyphenols as a bridge to bind RE elements and MFM, leading to stable loading and even distributions of RE elements, which is expected to provide excellent X-ray shielding performances.

### 3.3 Influence of dispersity on X-ray shielding performance

To examine the effect of dispersity on the X-ray shielding performance, the X-ray attenuation efficiency of the prepared samples was evaluated by a set of X-ray generating and detecting systems (Fig. 3a). According to the

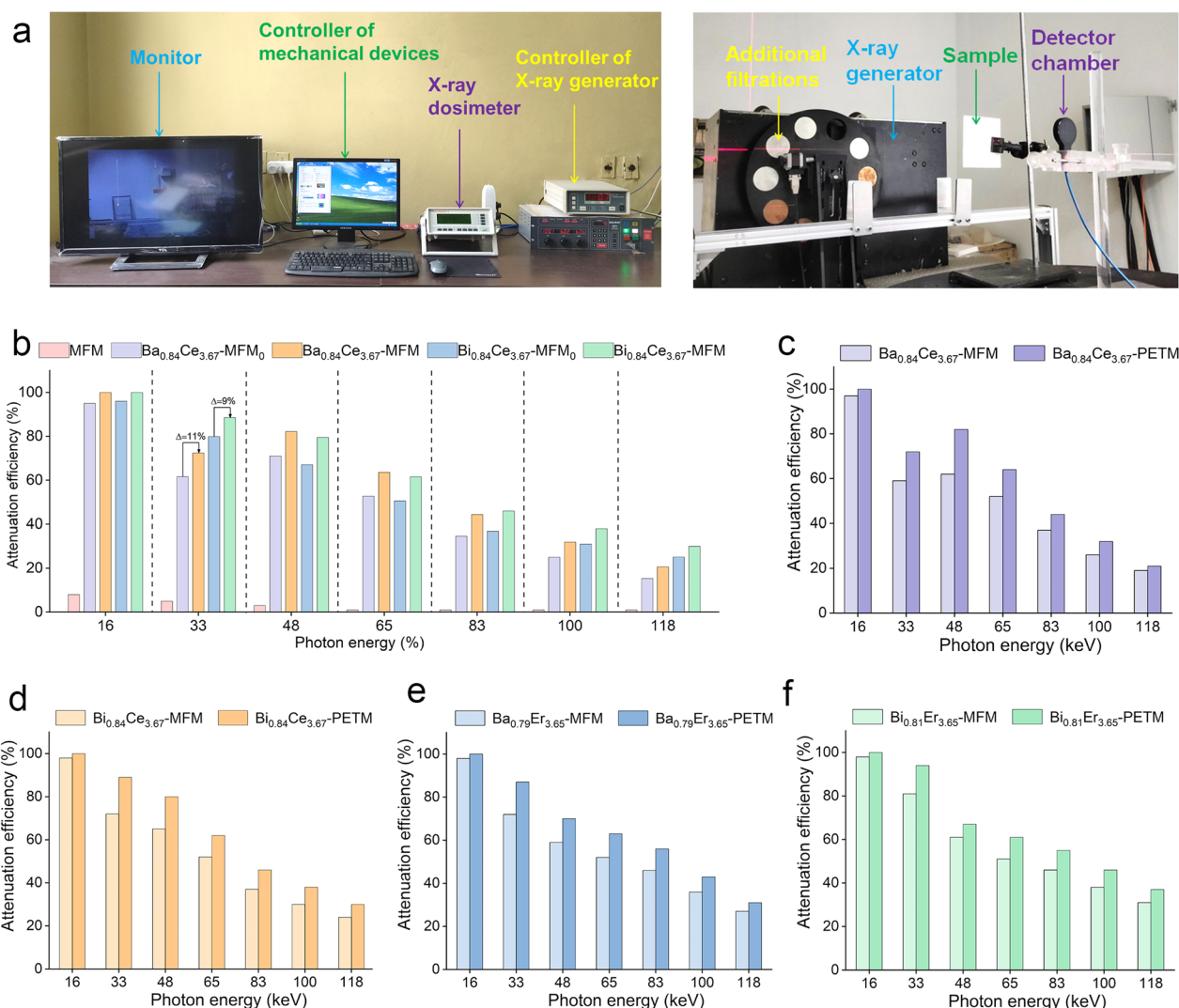


**Fig. 3** Influence of Dispersity on X-ray Shielding Performance. **a** Photographic demonstration of the X-ray generating and detecting setups. **b** X-ray attenuation efficiency of MFM,  $Ba_{0.84}Ce_{3.67}$ -MFM,  $Ba_{0.84}Ce_{3.67}$ -MFM<sub>0</sub>,  $Bi_{0.84}Ce_{3.67}$ -MFM<sub>0</sub> and  $Bi_{0.84}Ce_{3.67}$ -MFM. **c-f** X-ray attenuation efficiency of ZRE-MFM and ZRE-PETM,  $Ba_{0.84}Ce_{3.67}$ -MFM and  $Ba_{0.84}Ce_{3.67}$ -PETM (**c**),  $Bi_{0.84}Ce_{3.67}$ -MFM and  $Bi_{0.84}Ce_{3.67}$ -PETM (**d**),  $Ba_{0.79}Er_{3.65}$ -MFM and  $Ba_{0.79}Er_{3.65}$ -PETM (**e**),  $Bi_{0.81}Er_{3.65}$ -MFM and  $Bi_{0.81}Er_{3.65}$ -PETM (**f**)

measurement, the X-ray attenuation efficiency of MFM was only 8% at 16 keV and 5% at 33 keV, and dropped to zero as photon energy further increased, demonstrating that MFM provided little protection (Fig. 3b).

Additionally, X-ray attenuation properties of barium and cerium-containing composites with BT to facilitate the dispersion or without BT (noted as  $Ba_{0.84}Ce_{3.67}$ -MFM and  $Ba_{0.84}Ce_{3.67}$ -MFM<sub>0</sub>, respectively) were compared. As seen in Fig. 3b, although the two materials had the same Ba and Ce loading amounts,  $Ba_{0.84}Ce_{3.67}$ -MFM displayed approximately 10% superior X-ray attenuation efficiency compared to  $Ba_{0.84}Ce_{3.67}$ -MFM<sub>0</sub> when exposed to the incident X-ray with the same energy. With the addition

of BT, Ce was fully dispersed in MFM and its atoms were maximally accessible to the X-ray photons, enlarging the cross-section of the composites. According to our estimation, the enhancement of X-ray shielding performance stemming from the uniform dispersion of Ce was equivalent to increasing Ce loading amount from 0.91 to 1.81 mmol cm<sup>-3</sup>, indicating that the density of shielding materials could be reduced by improving the dispersity of high-Z elements. The same conclusion can be obtained from  $Bi_{0.84}Ce_{3.67}$ -MFM and  $Bi_{0.84}Ce_{3.67}$ -MFM<sub>0</sub> (Fig. 3b). Owing to the significant performance increase brought by the polyphenol-facilitated dispersion of high-Z elements, BT was utilized in all the samples to enhance the



X-ray shielding performance and reduce the material density.

The X-ray attenuation efficiency of ZRE-MFM and ZRE-PETM were compared to analyze the effect of the hierarchical structure on X-ray shielding performance. The attenuation efficiency of ZRE-MFM with the same elemental compositions and amounts was higher than that of ZRE-PETM in the range of 16–118 keV (Fig. 3c–f). According to our calculations, ZRE-MFM showed an averaged 9% and maximally 15% increase in X-ray attenuation efficiency compared with ZRE-PETM. In particular, the attenuation efficiency of  $\text{Ba}_{0.84}\text{Ce}_{3.67}$ -MFM was 20% higher than  $\text{Ba}_{0.84}\text{Ce}_{3.67}$ -PETM at 48 keV, providing compelling evidence of the benefit of hierarchical structure on X-ray shielding. As is well known, X-ray energy could be attenuated by the photoelectric effect and Compton scattering which transfer all or part of the energy to electron, respectively. The incident photons will predominantly interact with elements that are dispersed on the surface of nanoparticles, and few collisions will happen with elements distributed inside the particles. Therefore, the number of surficial RE elements need to be maximized to enhance the interact probability with X-rays, which calls for better dispersion of RE elements. MFM features the intriguing hierarchical structure, where multiple microfibers assemble into microfiber bundles and further into MFM. As mentioned before, the specific surface area of MFM is 6 times to that of PETM benefiting from its hierarchical structure. Therefore, MFM could expose more surfaces to evenly distribute RE element on the microfiber surface for better dispersion, increasing the number of atoms on the nanoparticle surface, enlarging the collision probability of RE element with photons. Additionally, the hierarchical pores between microfiber bundles and individual microfibers may elongate the transmission route of X-ray photons in the MFM to induce more interactions between photons and atoms of RE element as well as MFM, giving rise to extra attenuation of photon energy. In a word, the results of X-ray attenuation efficiency indicated that better dispersity stemming from the facilitation of BT and the hierarchical structure of MFM can provide benefits for X-ray shielding performances.

### 3.4 X-ray shielding performances of RE-MFM and ZRE-MFM

The single high-Z element displayed a distinct weak absorption region because X-ray with slightly lower energy than the absorption edge was incapable of interacting with electrons via the photoelectric effect [20, 37]. To address this issue, Ba or Bi was selected as the second high-Z element to compensate for the weak absorption regions of Ce and Er by coating. Considering

$\text{Bi}_{0.84}\text{Ce}_{3.67}$ -MFM as an example, the composite showed an excellent attenuation efficiency of 90% at 33 keV, which was 29% higher than that of  $\text{Ce}_{3.67}$ -MFM; and BiCe-MFM, BaEr-MFM and BiEr-MFM illustrated no obvious shielding defects in the whole range of 16–118 keV according to Additional file 1: Fig. S1. The result suggested that the weak absorption region of RE-MFM was successfully complemented through the synergistic effect of bis-high-Z elements. The detailed analysis of the synergistic effect of bis-high-Z elements on X-ray shielding can be seen in Supporting Information Sect. 1. Additionally, the attenuation efficiency of shielding materials is influenced by the K absorption edge of RE elements, resulting in a weak absorption region of shielding materials. In BaCe-MFM, due to the almost identical K absorption edges of Ba and Ce (37.44 and 40.45 keV, respectively), the overlapped weak absorption regions result in the inverted attenuation efficiency at 33 keV and 48 keV.

The X-ray shielding properties of ZRE-MFM were affected by RE loading amounts and material thickness [18]. For the same  $\text{Z}_{0.84}\text{Ce}_x$ -MFM sample, the attenuation efficiency showed an overall decreasing trend as the X-ray photon energy increased (Fig. 4a, d). All the composites could attenuate more than 90% of X-ray at 16 keV, whereas their efficiencies gradually diminished to around 20% at 118 keV. When X-ray photon energy was fixed, the attenuation efficiency increased with the increase of Ce contents. For X-ray at 48 keV, the attenuation efficiency of  $\text{Z}_{0.84}\text{Ce}_x$ -MFM rose by about 20% to more than 80% as the loading amount increased from 0.91 to 3.67 mmol  $\text{cm}^{-3}$ . Additionally, the shielding performance of the composites could be further elevated by increasing material thickness. It can be observed that when the X-ray photon energy was 100 keV, the attenuation efficiency of  $\text{Ba}_{0.84}\text{Ce}_{3.67}$ -MFM was substantially raised from an average value of 32% to 54% as the thickness increased from 1.4 to 2.8 mm (Fig. 4b). This was attributed to the enlarged collision probability of X-ray photons with uniformly dispersed RE elements in the elongated propagation path of the material. Further increase in the material thickness only resulted in 14% and 8% enhancement in attenuation efficiency, suggesting that the shielding performance enhancement was gradually limited as further increasing thickness. The same results were achieved for the attenuation properties of  $\text{Bi}_{0.84}\text{Ce}_{3.67}$ -MFM,  $\text{Ba}_{0.79}\text{Er}_{3.65}$ -MFM, and  $\text{Bi}_{0.81}\text{Er}_{3.65}$ -MFM (Fig. 4e and Additional file 1: Figs. S18–S21). Afterward, the linear attenuation coefficients (LAC) of  $\text{Z}_{0.84}\text{Ce}_{3.67}$ -MFM were obtained by fitting X-ray attenuation efficiencies versus material thicknesses according to the Lambert–Beer law [17]. The LACs of  $\text{Ba}_{0.84}\text{Ce}_{3.67}$ -MFM were 12.6, 7.3, 4.3, 2.8, and 1.7  $\text{cm}^{-1}$  at 48, 65, 83, 100, and 118 keV, respectively, which were reduced with the increasing

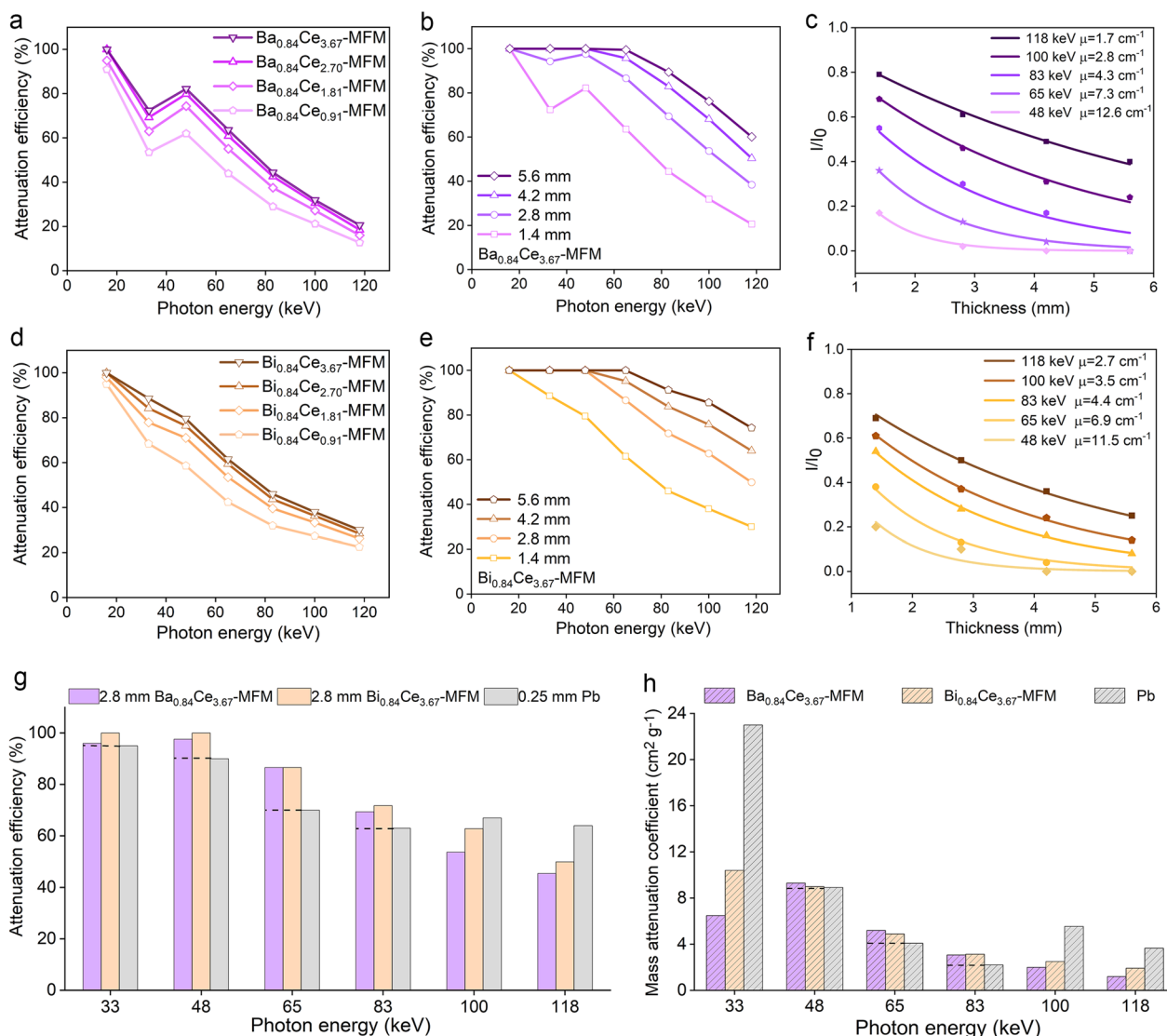


**Fig. 4** X-ray attenuation properties of RE-MFM and ZRE-MFM. **a** X-ray attenuation efficiency of  $Ba_{0.84}Ce_x$ -MFM with different Ce loadings. **b** X-ray attenuation efficiency of  $Ba_{0.84}Ce_{3.67}$ -MFM with different thicknesses. **c** The fitted curves of linear attenuation coefficients for  $Ba_{0.84}Ce_{3.67}$ -MFM at different energies. **d** X-ray attenuation efficiency of  $Bi_{0.84}Ce_x$ -MFM with different Ce loadings. **e** X-ray attenuation efficiency of  $Bi_{0.84}Ce_{3.67}$ -MFM with different thicknesses. **f** The fitted curves of linear attenuation coefficients for  $Bi_{0.84}Ce_{3.67}$ -MFM at different energies. **g** X-ray attenuation efficiency comparison of 2.8 mm  $Ba_{0.84}Ce_{3.67}$ -MFM, 2.8 mm  $Bi_{0.84}Ce_{3.67}$ -MFM, and 0.25 mm lead sheet. **h** Mass attenuation coefficients of  $Ba_{0.84}Ce_{3.67}$ -MFM,  $Bi_{0.84}Ce_{3.67}$ -MFM, and the lead sheet

X-ray photon energy (Fig. 4c). The same trend could be observed for  $Bi_{0.84}Ce_{3.67}$ -MFM and ZEr-MFM (Fig. 4f, Additional file 1: Figs. S22 and S23).

According to the Chinese National Standard GB 16,757–2016, materials with X-ray shielding performance no less than that of 0.25 mm lead are considered potential materials for producing X-ray protecting suits [38]. Therefore, a 0.25 mm lead sheet was chosen as the reference standard for assessing the X-ray shielding

performance. Based on the measurements, the overall X-ray shielding performance of 2.8 mm  $Zr_{0.84}Ce_{3.67}$ -MFM surpassed that of the 0.25 mm lead sheet in the range of 33–83 keV (Fig. 4g). Note that  $Zr_{0.84}Ce_{3.67}$ -MFM exhibited outstanding X-ray shielding performance, prohibiting 90% of incident X-rays at 65 keV and displaying 20% enhancement as compared to the 0.25 mm lead sheet. Moreover, the mass attenuation coefficients (MACs) of the materials were calculated using Eq. 3. The MACs

of  $Z_{0.84}Ce_{3.67}$ -MFM exceeded those of the lead sheet in 48–83 keV (Fig. 4h), and were still 40% greater than those of the lead even the X-ray energy was as high as 83 keV. Additionally, the MAC values of some polymer-based X-ray shielding materials are summarized in Table 1. It can be observed that microfiber membrane-based X-ray shielding materials displayed superior shielding performance at low bulk density, demonstrating the merit of polyphenol- and hierarchical structure-facilitated dispersion. In summary, ZRE-MFM with evenly dispersed high-Z elements showed excellent X-ray shielding performance and exhibited promising application potentials in various scenarios.

### 3.5 Physical and mechanical properties of ZRE-MFM

Both remarkable X-ray shielding performance and outstanding physiomechanical behaviors are indispensable prerequisites of advanced X-ray shielding materials for versatile applications [19], thus, the mechanical and physical properties of BiCe-MFM are assessed as a demonstration in this section. MFM displayed prominent tensile strength of  $9.9 \text{ N mm}^{-2}$  and tear strength of  $58.5 \text{ N mm}^{-1}$  stemming from its three-dimensional hierarchical structure (Fig. 5a, b). Without rupturing the original structure of MFM when loading RE elements by the “impregnation–desolvation” strategy, Ce-MFM fully retained the excellent mechanical performance of MFM. Surprisingly, BiCe-MFM showed superior tensile strength and tear strength ( $11.5 \text{ N mm}^{-2}$  and  $65.1 \text{ N mm}^{-1}$ , respectively) due to the strengthening effect of the introduced waterborne polyurethane (WPU) thin film on the Ce-MFM surface, which were around 4.5 times and 2 times compared with those of the 0.25 mm lead sheet ( $2.6 \text{ N mm}^{-2}$  and  $28.2 \text{ N mm}^{-1}$ , respectively). The corresponding stress–strain curves and load–extension curves of MFM, Ce-MFM and BiCe-MFM were shown in Additional file 1: Figs. S24 and S25. Besides, the as-prepared X-ray shielding material displayed an ultralow density of  $1.4 \text{ g cm}^{-3}$ , only 1/8 of that of the lead

( $11.3 \text{ g cm}^{-3}$ ), exhibiting great potential in the mobile application conditions (Fig. 5c). Wearable shielding materials need to have good fastness properties to washing, rubbing and bending, thus, the attenuation efficiency of  $Bi_{0.84}Ce_{3.67}$ -MFM was tested after rubbing 10,000 times, bending 5,000 times and soaking in water (Fig. 5d–f), the processes of testing were shown in Additional file 1: Figs. S26–28. As shown in Fig. 5g–i, the results exhibited negligible reduction of attenuation efficiency, indicating that the as-prepared shielding materials obtained outstanding fastness properties to soaking, rubbing and bending. In a word, the prepared microfiber membrane-based X-ray shielding materials exhibited outstanding physical and mechanical properties and were appropriate for a variety of application environments.

## 4 Conclusion

In summary, with the assistance of plant polyphenols, we successfully prepared high-performance X-ray shielding materials based on microfiber membrane, a type of synthetic leather. With the addition of BT to facilitate the dispersion of RE element, the as-prepared materials exhibited an average 10% superior X-ray attenuation efficiency compared to the composites without the addition of polyphenol; meanwhile, the hierarchical structure of MFM provided larger specific surface area to load and disperse RE element, leading to an extra enhancement of average 9% on the X-ray shielding performance. Benefiting from synergistic effect of hierarchical structure and plant polyphenol, the obtained ZRE-MFM with uniformly dispersed RE element exhibited 19% increase in X-ray attenuation efficiency, and displayed higher MACs than that of lead sheet in 48–83 keV. In particular, the MAC of  $Bi_{0.84}Ce_{3.67}$  was 40% larger than that of the lead at 83 keV. Furthermore, the prepared composites had an ultralow density of  $1.4 \text{ g cm}^{-3}$ , which was as low as 1/8 of that of the lead, while retained outstanding physical and mechanical properties. Our study would shed new light on the manufacture of novel X-ray shielding materials with excellent X-ray shielding performance.

**Table 1** The X-ray shielding performance of polymer matrix based shielding materials

No	Polymer matrix	High-Z elements	Density ( $\text{g cm}^{-3}$ )	Incident X-ray	Mass attenuation coefficient ( $\text{cm}^2 \text{g}^{-1}$ )	References
1	Polystyrene	Ba	1.68	50 keV	3.9	[12]
2	Wood/Polyvinyl chloride	Bi	2.04	60 kVp	2.2	[39]
3	Silicone rubber	W	2.55	100 kVp	0.5	[40]
4	Polyvinyl chloride	Ta and Bi	1.66	129 kVp	2.7	[41]
5	Microfiber membrane	Ce and Ba	1.40	48 keV	9.0	This work
6	Microfiber membrane	Ce and Bi	1.40	83 keV	3.2	This work
7	Microfiber membrane	Ce and Bi	1.40	100 keV	2.5	This work

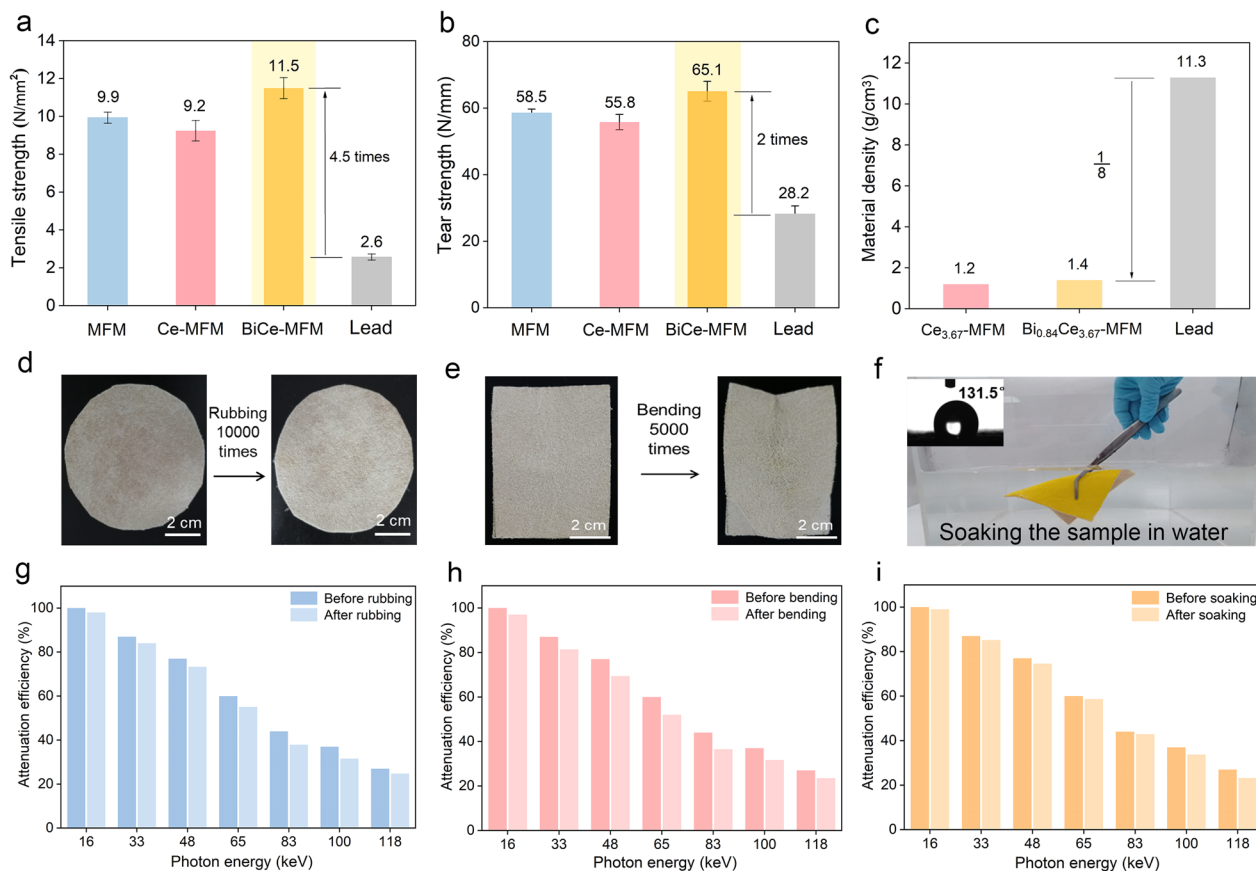


**Fig. 5** Mechanical and physical properties of as-prepared composites. **a–b** Tensile strength **(a)** and tear strength **(b)** of MFM, Ce-MFM, BiCe-MFM, and lead sheet. **c** Material density of Ce<sub>3,67</sub>-MFM, Bi<sub>0,84</sub>Ce<sub>3,67</sub>-MFM, and lead sheet. **d** The digital photograph of BiCe-MFM before and after rubbing 10,000 times. **e** The digital photograph of BiCe-MFM before and after bending 5,000 times. **f** The soaking process of BiCe-MFM. **g–i** X-ray attenuation efficiency of Bi<sub>0,84</sub>Ce<sub>3,67</sub>-MFM before and after rubbing 10,000 times **(g)**, bending 5,000 times **(h)** and soaking **(i)**

**Abbreviations**

Z	Atomic number
MFM	Microfiber membrane
RE	Rare earth element
NPs	Nanoparticles
PETM	Woven polyethylene terephthalate fabric membrane
MPN	Metal–phenolic networks
RE-MPN	Rare earth metal–phenolic networks
BT	Bayberry tannin
WPU	Waterborne polyurethane
ZRE-MFM	Bis-high-Z element composites based on microfiber membrane
RE-MFM	Rare earth element composites based on microfiber membrane
ZRE-PETM	Bis-high-Z element composites based on woven polyethylene terephthalate fabric membrane
ZRE-MFM <sub>0</sub>	Bis-high-Z element composites based on microfiber membrane without bayberry tannin
MAC	Mass attenuation coefficient
LAC	Linear attenuation coefficient

**Supplementary Information**

The online version contains supplementary material available at <https://doi.org/10.1186/s42825-023-00119-5>

**Additional file 1. Section 1:** Synergistic effect of bis-high-Z elements on X-ray shielding. **Section 2:** Supplementary Figures. **Section 3:** Supplementary Tables. **Section 4:** References.

**Acknowledgements**

This work is supported by the National Natural Science Foundation of China (Grant No. 21878191) and Wende Innovation Research Institute of Waterborne Microfiber and Leather. Additionally, the authors are grateful for Mr. Wenlong Dong from the National Institute of Measurement and Testing Technology of China for his kind assistance in measuring the X-ray attenuation properties. And we would like to thank Dr. Ying Song at College of Biomass Science and Engineering, Sichuan University, for the technical assistance. Moreover, the authors would like to express their gratitude to EditSprings (<https://www.editsprings.cn>) for the expert linguistic services provided.

**Author contributions**

BS, XL and YW conceived the idea and supervised the project. LY, JZ and HL conducted the experiments. LY carried out the characterizations and tests with the techniques provided by RZ, JZ and XX, and analyzed the data. LY drafted the original manuscript. YW performed the data visualization and revised the manuscript. XL and BS provided the funding supports. All authors read and approved the final manuscript.

**Funding**

The National Natural Science Foundation of China (No. 21878191).

**Availability of data and materials**

All data generated or analyzed during this study are included in this published article.

**Declarations****Ethics approval and consent to participate**

This research was based on the results of experiment and no ethics approval was required and no human or animal subjects were involved in the research.

**Consent for publication**

The authors provide consent for publication of this paper in the journal.

**Competing interests**

The authors declare that they have no known competing financial interests or personal relationships that could have appeared to influence the work reported in this paper.

**Author details**

<sup>1</sup>College of Biomass Science and Engineering, Sichuan University, Chengdu 610065, People's Republic of China. <sup>2</sup>National Engineering Laboratory for Clean Technology of Leather Manufacture, Sichuan University, Chengdu 610065, People's Republic of China. <sup>3</sup>Key Laboratory of Radiation Physics and Technology, Ministry of Education Institute of Nuclear Science and Technology, Sichuan University, Chengdu 610065, People's Republic of China. <sup>4</sup>Mingxin Automotive Leather Co., Ltd., Jiaying 314006, People's Republic of China. <sup>5</sup>Department of Chemistry, Materials Innovation Factory, University of Liverpool, Liverpool L7 3NY, UK.

Received: 14 February 2023 Revised: 6 April 2023 Accepted: 10 April 2023  
Published online: 21 April 2023

**References**

- Cunningham R, Zhao C, Parab N, Kantzos C, Pauza J, Fezzaa K, Sun T, Rollett AD. Keyhole threshold and morphology in laser melting revealed by ultrahigh-speed X-ray imaging. *Science*. 2019;363(6429):849–52. <https://doi.org/10.1126/science.aav4687>.
- Mara MW, Hadt RG, Reinhard ME, Kroll T, Lim H, Hartsock RW, Alonso-Mori R, Chollet M, Glownia JM, Nelson S, Sokaras D, Kunnus K, Hodgson KO, Hedman B, Bergmann U, Gaffney KJ, Solomon EI. Metalloprotein entatic control of ligand-metal bonds quantified by ultrafast X-ray spectroscopy. *Science*. 2017;356(6344):1276–80. <https://doi.org/10.1126/science.aam6203>.
- Kim J, Kim J, Lim J, Lee S, Lee C, Hong S. Cold-cathode X-ray irradiation pre-treatment for fouling control of reverse osmosis (RO) in shale gas produced water (SGPW) treatment. *Chem Eng J*. 2019;374:49–58. <https://doi.org/10.1016/j.cej.2019.05.158>.
- Zhang KQ, Meng QY, Zhang XQ, Qu ZL, He RJ. Quantitative characterization of defects in stereolithographic additive manufactured ceramic using X-ray computed tomography. *J Mater Sci Technol*. 2022;118:144–57. <https://doi.org/10.1016/j.jmst.2021.11.060>.
- Applegate KE, Amis ES, Schauer DA. Radiation exposure from medical imaging procedures. *N Engl J Med*. 2009;361(23):2289–92. <https://doi.org/10.1056/NEJMc0909579>.
- Li Q, Ding PP, Wang YP, Liao XP, Shi B. Preparation of a rare earth natural leather X-ray protection material and its properties. *Acta Phys-Chim Sin*. 2021;37(10):2001046. <https://doi.org/10.3866/PKU.WHXB202001046>.
- Yu SB, Watson AD. Metal-based X-ray contrast media. *Chem Rev*. 1999;99(9):2353–78. <https://doi.org/10.1021/cr980441p>.
- Lee N, Choi SH, Hyeon T. Nano-sized CT contrast agents. *Adv Mater*. 2013;25(19):2641–60. <https://doi.org/10.1002/adma.201300081>.
- Christodoulou EG, Goodsitt MM, Larson SC, Darner KL, Satti J, Chan HP. Evaluation of the transmitted exposure through lead equivalent aprons used in a radiology department, including the contribution from backscatter. *Med Phys*. 2003;30(6):1033–8. <https://doi.org/10.1118/1.1573207>.
- Aral N, Nergis FB, Candan C. An alternative X-ray shielding material based on coated textiles. *Text Res J*. 2016;86(8):803–11. <https://doi.org/10.1177/0040517515590409>.
- Muthamma MV, Bubbly SG, Gudennavar SB, Narendranath KCS. Poly(vinyl alcohol)-bismuth oxide composites for X-ray and  $\gamma$ -ray shielding applications. *J Appl Polym Sci*. 2019;136(37):47949. <https://doi.org/10.1002/app.47949>.
- Jaiyen S, Phunpueok A, Thongpool V. Determination of radiation attenuation coefficients of BaSO<sub>4</sub>/PVC and BaSO<sub>4</sub>/PS for X-ray shielding. *J Phys Conf Ser*. 2019;1380:012133. <https://doi.org/10.1088/1742-6596/1380/1/012133>.
- Xu CJ, Tung GA, Sun SH. Size and concentration effect of gold nanoparticles on X-ray attenuation as measured on computed tomography. *Chem Mater*. 2008;20(13):4167–9. <https://doi.org/10.1021/cm8008418>.
- Lopresti M, Palin L, Alberto G, Cantamessa S, Milanesio M. Epoxy resins composites for X-ray shielding materials additivated by coated barium sulfate with improved dispersibility. *Mater Today Commun*. 2021;26:101888. <https://doi.org/10.1016/j.mtcomm.2020.101888>.
- Yu RR, Pei XY, Sun LW, Xia YH, Liu SK, Liu D, Chen L, Tang YH, Xu ZW, Liu LS, Wang W. <sup>1</sup>CoFe/C nanosheets on hollow carbon fibers as composite fabrics for electromagnetic interference shielding. *ACS Appl Nano Mater*. 2022;5(8):11665–78. <https://doi.org/10.1021/acsnm.2c02642>.
- Tas M, Musa UG, Ahmed I, Xu F, Smartt C, Hou XH. Functionalised SiO<sub>2</sub> modified icephobic nanocomposite electrospun membranes for outdoor electromagnetic shielding applications. *Polymer*. 2022;240:124499. <https://doi.org/10.1016/j.polymer.2021.124499>.
- Quan JY, Wang HQ, Yu JR, Wang Y, Zhu J, Hu ZM. UHMWPE/nanoparticle composite membrane for personal radiation shielding. *Compos Sci Technol*. 2021;201:108500. <https://doi.org/10.1016/j.compscitech.2020.108500>.
- Wang YP, Zhong R, Li Q, Liao JL, Liu N, Joshi NS, Shi B, Liao XP, Guo JL. Lightweight and wearable X-ray shielding material with biological structure for low secondary radiation and metabolic saving performance. *Adv Mater Technol*. 2020;5(7):2000240. <https://doi.org/10.1002/admt.20200240>.
- Wang YP, Ding PP, Xu H, Li Q, Guo JL, Liao XP, Shi B. Advanced X-ray shielding materials enabled by the coordination of well-dispersed high atomic number elements in natural leather. *ACS Appl Mater Interfaces*. 2020;12(17):19916–26. <https://doi.org/10.1021/acami.0c01663>.
- Shen Y, Zhou JB, Han Z, Li H, Yan LP, Liao XP, Shi B. Natural leather based gamma-ray shielding materials enabled by the coordination of well-dispersed Bi<sup>3+</sup>/Ba<sup>2+</sup> ions and RE<sub>2</sub>O<sub>3</sub> coating. *J Leather Sci Eng*. 2022;4:15. <https://doi.org/10.1186/s42825-022-00090-7>.
- Wang DH, Zhang TJ, Zhang DJ, Bao JW, Liu ZJ. Study on the poly (ether sulfone) microfibrils. *Appl Mech Mater*. 2013;395:419–411. <https://doi.org/10.4028/www.scientific.net/AMM.395-396.419>.
- Geng HM, Zhong QZ, Li JH, Lin ZX, Cui JW, Caruso F, Hao JC. Metal ion-directed functional metal-phenolic materials. *Chem Rev*. 2022;122(13):11432–73. <https://doi.org/10.1021/acs.chemrev.1c01042>.
- General administration of quality supervision, inspection and quarantine of the People's Republic of China, X and Gamma radiation dose equivalent (rate) meters and monitors used in radiation protection, 2003.
- Viegas J, Silva LA, Batista AMS, Furtado CA, Nascimento JP, Faria LO. Increased X-ray attenuation efficiency of graphene-based nanocomposite. *Ind Eng Chem Res*. 2017;56(41):11782–90. <https://doi.org/10.1021/acs.iecr.7b02711>.
- Issa SAM, Saddeek YB, Sayyed MI, Tekin HO, Kilicoglu O. Radiation shielding features using MCNPX code and mechanical properties of the PbONa<sub>2</sub>OB<sub>2</sub>O<sub>3</sub>CaOAl<sub>2</sub>O<sub>3</sub>SiO<sub>2</sub> glass systems. *Compos Part B Eng*. 2019;167:231–40. <https://doi.org/10.1016/j.compositesb.2018.12.029>.
- Kim Y, Park S, Seo Y. Enhanced X-ray shielding ability of polymer-non-leaded metal composites by multilayer structuring. *Ind Eng Chem Res*. 2015;54(22):5968–73. <https://doi.org/10.1021/acs.iecr.5b00425>.
- Noor Azman NZ, Siddiqui SA, Low IM. Characterisation of micro-sized and nano-sized tungsten oxide-epoxy composites for radiation shielding of diagnostic X-rays. *Mater Sci Eng C*. 2013;33(8):4952–7. <https://doi.org/10.1016/j.msec.2013.08.023>.
- Guo JL, Tardy BL, Christofferson AJ, Dai YL, Richardson JJ, Zhu W, Hu M, Ju Y, Cui JW, Dagastine RR, Yarovsky I, Caruso F. Modular assembly of superstructures from polyphenol-functionalized building blocks. *Nat Nanotechnol*. 2016;11(12):1105–11. <https://doi.org/10.1038/nnano.2016.172>.
- Guo JL, Ping Y, Ejima H, Alt K, Meissner M, Richardson JJ, Yan Y, Peter K, von Elverfeldt D, Hagemeyer CE, Caruso F. Engineering multifunctional

- capsules through the assembly of metal–phenolic networks. *Angew Chem Int Ed*. 2014;53(22):5546–51. <https://doi.org/10.1002/anie.201311136>.
30. Ejima H, Richardson JJ, Liang K, Best JP, van Koeverden MP, Such GK, Cui JW, Caruso F. One-step assembly of coordination complexes for versatile film and particle engineering. *Science*. 2013;341(6142):154–7. <https://doi.org/10.1126/science.1237265>.
  31. An L, Cai Y, Tian QW, Lin JM, Yang SP. Ultrasensitive iron-based magnetic resonance contrast agent constructed with natural polyphenol tannic acid for tumor theranostics. *Sci China Mater*. 2021;64(2):498–509. <https://doi.org/10.1007/s40843-020-1434-1>.
  32. Guo JL, Wang XX, Miao PL. One-step seeding growth of controllable Ag@Ni core–shell nanoparticles on skin collagen fiber with introduction of plant tannin and their application in high-performance microwave absorption. *J Mater Chem*. 2012;22(24):11933–42. <https://doi.org/10.1039/c2jm31710a>.
  33. Lapuente R, Quijada C, Huerta F, Cases F, Vázquez JL. X-ray photoelectron spectroscopy study of the composition of polyphenol films formed on Pt by electropolymerisation of phenol in the presence of sulphide in carbonate medium. *Polym J*. 2003;35(12):911–9. <https://doi.org/10.1295/polymj.35.911>.
  34. Qi FW, Gao XW, Shuai Y, Peng SP, Deng YW, Yang S, Yang YW, Shuai CJ. Magnetic-driven wireless electrical stimulation in a scaffold. *Compos Part B Eng*. 2022;237:109864. <https://doi.org/10.1016/j.compositesb.2022.109864>.
  35. Lv YR, Wang ZL, Yang YX, Luo Y, Yang SY, Xu YH. Tin bisulfide nanoplates anchored onto flower-like bismuth tungstate nanosheets for enhancement in the photocatalytic degradation of organic pollutant. *J Hazard Mater*. 2022;432:128665. <https://doi.org/10.1016/j.jhazmat.2022.128665>.
  36. Oh HI, Hoff JE, Armstrong GS, Haff LA. Hydrophobic interaction in tannin-protein complexes. *J Agric Food Chem*. 1980;28(2):394–8. <https://doi.org/10.1021/jf60228a020>.
  37. McCaffrey JP, Shen H, Downton B, Mainegra-Hing E. Radiation attenuation by lead and nonlead materials used in radiation shielding garments: radiation attenuation by radiation shielding garments. *Med Phys*. 2007;34(2):530–7. <https://doi.org/10.1118/1.2426404>.
  38. General administration of quality supervision, inspection and quarantine of the People's Republic of China, standardization administration of the People's Republic of China, protective clothing—X-ray protective clothing, 2016. <https://openstd.samr.gov.cn/bzgk/gb/newGblInfo?hcno=707A563DE3E4692E33A5205C36F8506E>
  39. Poltabtim W, Wimolmala E, Markpin T, Sombatsompop N, Rosarpitak V, Saenboonruang K. X-ray shielding, mechanical, physical, and water absorption properties of wood/PVC composites containing bismuth oxide. *Polymers*. 2021;13(13):2212. <https://doi.org/10.3390/polym13132212>.
  40. Aral N, Nergis FB, Candan C. The X-ray attenuation and the flexural properties of lead-free coated fabrics. *J Ind Text*. 2017;47(2):252–68. <https://doi.org/10.1177/1528083716644287>.
  41. Nuñez-Briones AG, Benavides R, Bolaina-Lorenzo ED, Martínez-Pardo ME, Kotzian-Pereira-Benavides C, Mendoza-Mendoza E, Bentacourt-Galindo R, García-Cerda LA. Nontoxic flexible PVC nanocomposites with Ta<sub>2</sub>O<sub>5</sub> and Bi<sub>2</sub>O<sub>3</sub> nanoparticles for shielding diagnostic X-rays. *Radiat Phys Chem*. 2023;202:110512. <https://doi.org/10.1016/j.radphyschem.2022.110512>.

## Publisher's Note

Springer Nature remains neutral with regard to jurisdictional claims in published maps and institutional affiliations.

Submit your manuscript to a SpringerOpen<sup>®</sup> journal and benefit from:

- Convenient online submission
- Rigorous peer review
- Open access: articles freely available online
- High visibility within the field
- Retaining the copyright to your article

---

Submit your next manuscript at ► [springeropen.com](https://www.springeropen.com)

---